universität wien

MASTERARBEIT / MASTER'S THESIS

Titel der Masterarbeit / Title of the Master's Thesis

„Thermal coupling in the Perseus molecular cloud“

verfasst von / submitted by

Markus Ambrosch, BSc

angestrebter akademischer Grad / in partial fulfilment of the requirements for the degree of

Master of Science (MSc)

Wien, 2017 / Vienna 2017

Studienkennzahl lt. Studienblatt / degree programme code as it appears on the student record sheet:	A 066 861
Studienrichtung lt. Studienblatt / degree programme as it appears on the student record sheet:	Astronomie
Betreut von / Supervisor:	Univ.-Prof. João Alves, PhD

Abstract

This work observationally investigates the thermal coupling of gas and dust in molecular cloud cores which is frequently assumed in thermal balance calculations of cores but is yet poorly confirmed by observations. For this purpose the gas kinetic temperatures, derived from ammonia line observations, and dust effective temperatures of 153 cloud cores in the Perseus molecular cloud are compared. This comparison confirms the effect of thermal coupling predicted by Goldsmith (2001) that at densities above $n(H_2) \approx 10^4$ cm^{-3} the gas temperatures do not rise but converge towards the dust temperatures. Above a density of $n(H_2) = 10^5$ cm^{-3} the gas kinetic and dust effective temperatures of cloud cores are within 5 K. There is a linear correlation between the gas kinetic and dust effective temperature but one has to be careful when deriving the gas temperature from the dust effective temperature because these are strongly affected by temperature gradients along the line of sight caused by environmental effects. Embedded protostars inside the cloud cores do not significantly affect the effective dust temperatures.

Zusammenfassung

Diese Arbeit untersucht die thermische Kopplung von Gas und Staub in dichten Kernen von Molekülwolken. Diese thermische Kopplung findet in theoretischen Modellen zu Wolkenkernen häufig Anwendung, ist aber noch unzureichend durch Beobachtungen bestätigt. Zu diesem Zweck wird die kinetische Temperatur des Gases, bestimmt durch Beobachtungen von Ammoniak-Linien, und die effektive Staubtemperatur von 153 Wolkenkernen in der Perseus-Molekülwolke verglichen. Der Vergleich bestätigt den von Goldsmith (2001) vorhergesagten Effekt der thermischen Kopplung, dass die Gastemperaturen bei Dichten über $n(H_2) \approx 10^4$ cm^{-3} nicht ansteigen, sondern sich den Staubtemperaturen annähern. Bei Dichten ber $n(H_2) = 10^5$ cm^{-3} ist der Unterschied zwischen den Gastemperaturen und effektiven Staubtemperaturen der Wolkenkerne kleiner als 5 K. Es besteht eine lineare Korrelation zwischen den Gastemperaturen und effektiven Staubtemperaturen aber bei der Berechnung der Gastemperaturen aus den effektiven Staubtemperaturen ist Vorsicht geboten, da diese stark von Temperaturgradienten entlang der Sichtlinie abhängen, welche von Umgebungseinflüssen hervorgerufen werden. Eingebettete Protosterne in den Wolkenkernen hingegen haben keinen gravierenden Effekt auf die effektive Staubtemperaturen der Wolkenkerne.

Aknowledgement

I would like to thank my supervisor João Alves for his support and useful comments that helped me finishing this thesis. Furthermore I would like to express my gratitude to Alvaro Hacar and Jan Forbrich for introducing me to the topic and guiding me along the way. Last but foremost I would like to thank my parents for their moral and financial support throughout all these years. Without them this thesis would not exist.

Danke.

Inhaltsverzeichnis

1 Introduction

Molecular clouds are the main location of star formation in the Milky Way. Understanding the physical processes that govern the conditions in molecular clouds is therefore crucial to understand how stars form. One aspect that affects star formation directly is the thermal balance that determines the temperature in molecular clouds. Dust and molecular gas, which are the main components of molecular clouds, generally get heated respectively cooled by independent processes and the result are different temperatures of the gas and dust. At high densities however, collisions between gas and dust particles become frequent enough that the two phases can exchange thermal energy and their temperatures are no longer independent. Following a model for the exchange of kinetic energy between gas and dust particles by Burke & Hollenbach (1983), Goldsmith (2001) calculated the effects of this *thermal coupling* by using a radiative transfer model. Above a certain density the gas and dust temperatures start to approach each other until they are essentially equal at the highest densities. These theoretical results by Goldsmith are widely used in works that deal with the thermal balance in molecular clouds and especially cloud core models (e.g. Galli et al. 2002; Gonçalves et al. 2004; Sipilä et al. 2016) but observationally the thermal coupling is not well investigated. Comparisons of gas temperatures from ammonia (NH_3) observations and dust effective temperatures in dense cloud cores in the Pipe Nebula indicate that there is a linear relationship between the two temperatures (Forbrich et al. 2014). Considering the small sample of only nine cloud cores investigated in the Pipe Nebula, a comparison of gas and dust temperatures in a larger sample of cores seems appropriate. The aim of this thesis is therefore to compare the gas and dust temperatures in an extended sample of cloud cores to verify the theoretical effects of thermal coupling. A second goal is to investigate if a possible linear relationship between the gas and dust effective temperatures can be used to determine the gas temperature in cloud cores only from measurements of the dust effective temperature which

cost less effort to be obtained.
Section 2 describes the thermal balance in molecular clouds and the effects that thermal coupling is predicted to have on the gas and dust temperatures. Based on ammonia observations it is shown in Sections 3 and 4 that the threshold density required for thermal coupling is reached in molecular cloud cores. Section 5 describes how NH_3 kinetic temperatures and dust effective temperatures are determined from observations and in Section 6 gas and dust effective temperatures of a sample of Perseus cores are compared and investigated for thermal coupling.

2 Thermal balance in molecular clouds

There are several processes that regulate the gas and dust temperatures in molecular clouds. At low densities the gaseous and dusty phase of the interstellar medium are heated respectively cooled by independent processes and they do not affect each other. Therefore, at low densities, there is no correlation between the gas and dust temperatures.

2.1 Gas temperature

The temperature of an ensemble of gas particles (atoms or molecules) is a measure for the average kinetic energy of the gas particles. This *kinetic* gas temperature of a gas that consists of particles of mass m is defined as

$$T_{kin} = \frac{m\overline{v}^2}{3k}. \tag{1}$$

In an ideal gas the velocities of the individual gas particles follow a Maxwell-distribution and the kinetic temperature depends on the mean particle velo-

city $\overline{v}$ (k is Boltzmann's constant). Processes that affect the average kinetic energy of gas particles therefore lead to a change of the gas temperature.
In molecular clouds the main heating process for the gas are collisions of high energy cosmic rays, originating from outside the clouds or from embedded young stellar objects (YSOs), with the gas particles. This causes the ionization of the gas particle and the kinetic energy of the ejected electrons lead to the heating of the gas. Heating by photoionization in contrast is negligible in the dense regions of molecular clouds, because most of the photos that have enough energy to ionize the molecular gas are absorbed in the outer regions of the clouds.
Gas cools by line emission from molecules. Since the most abundant molecule H_2 shows almost no emission at low temperatures, the major coolant in cold molecular clouds is CO (Goldsmith & Langer 1978). The optical depths of the cooling emission lines can be large (the CO(1-0) line for example is typically optically thick in molecular clouds). Because of this the cooling radiation can not leave the clouds directly and radiative transfer models are necessary to calculate the gas cooling rates.

2.2 Dust temperature

Contrary to the gas kinetic temperature, there is no thermodynamically defined measure of the temperature of an ensemble of dust grains. The temperature of each individual dust grain is instead a measure of the mean vibrational energies of atoms or molecules in the grain's particle lattice. These vibrations lead to the emission of a blackbody spectrum and by observing this radiation the temperature of a dust grain can be measured. Because the number and energy distribution of these vibrational states depend for example on the particle size and chemical composition, individual dust grains will have different temperatures even if they are in the same physical environment.
Dust is primarily heated by the photons of the interstellar radiation field (ISRF) with typical wavelengths between the UV and IR. While most of these

photons are absorbed by dust grains in the outer layers of molecular clouds and thus heat those areas effectively, only a fraction of the heating photons reach the inner regions of the clouds. This ättenuationöf the radiation field results in a gradient of the average dust temperature, from warmer outer layers to low temperatures in the dense cloud cores.
Dust cools by thermal emission of the grains. At the low dust temperatures in molecular clouds of typically 10 - 20 K, the peak of this continuum emission is in the far infrared (FIR). Because the absorption cross-section of dust grains for photons in this wavelength-range is small, the clouds are optically thin to dust-emission. Heating of the dust by absorption of re-radiation from dust grains can therefore be neglected (Goldsmith 2001).

Thermal balance calculations that consider only these heating and cooling processes, result in independent gas and dust temperatures in molecular clouds, where the gas temperatures are typically higher than the dust temperatures (Goldsmith 2001).

2.3 Thermal coupling

Above a certain density the gas and dust phase start to thermally influence each other and their temperatures are no longer independent. This thermal coupling of gas and dust happens because at high densities collisions between gas and dust particles and therefore the transfer of kinetic energy between the two phases becomes frequent (Burke & Hollenbach 1983). Considering that H_2 represents almost the entire content of molecular gas in space, the rate per unit volume at which kinetic energy is transferred from gas to dust particles by collisions can be written as

$$\Lambda_{gd} = n(\mathrm{H_2}) n_d \langle \sigma_d v_{\mathrm{H_2}} \rangle \alpha (2kT_{gas} - 2kT_{dust}) \tag{2}$$

where $n(H_2)$ and n_d are the number densities of H_2 respectively dust particles and $\langle \sigma_d v_{H_2} \rangle$ is the collision rate, averaged over all gas particle-velocities v_{H_2} and the collision cross-sections of dust grains σ_d which vary with the grain size. The velocities of the dust particles are assumed to vary according to a Maxwell-distribution and then the term in brackets is the difference in average kinetic energy of the gas and dust particles at temperatures T_{gas} respectively T_{dust}. Generally, not all of the kinetic energy of a gas particle is transferred to the dust in a collision and the accommodation coefficient α accounts for that. It is defined that $\alpha = 1$ when the gas and dust particles have the same kinetic energy after a collision (Burke & Hollenbach 1983).

2.4 Thermal balance with thermal coupling

Considering all the before mentioned heating and cooling mechanisms, including the thermal coupling, Goldsmith (2001) calculated typical gas and dust temperatures in molecular clouds by using a radiative transfer model. Figure 1 shows the effect of including thermal coupling in the thermal balance calculations for molecular clouds. When only the independent heating and cooling mechanisms mentioned in Sections 2.1 and 2.2 are included in the model, the gas and dust temperatures start to diverge at densities above $n(H_2) \approx 10^4$ cm^{-3}. With increasing density, collisions of cosmic rays with the gas particles become more frequent and the gas is heated efficiently. At the same time the cooling rate of the gas decreases because the optical depth of important cooling lines (e.g. from CO and HCO^+) becomes larger. This leads to an increasing gas temperature at increasing densities. On the other hand, the interstellar radiation field that heats the dust is largely absorbed by the outer cloud layers even at lower densities. Contrary to the gas, the dust temperature is therefore not very sensitive to the density in the cloud. This behavior changes when collisions between gas and dust particles are included in the radiative transfer calculations. Instead of rising, the gas temperature now declines towards the dust temperature with rising density. This

is because the dust now cools the gas via the thermal coupling. The dust in turn is heated by the gas and the temperatures of the two phases converge and become essentially equal at $n(H_2) \approx 10^6$ cm^{-3}. Note that the thermal coupling rises the dust temperature by only 1 – 2 K while the gas temperature is reduced by approximately 15 K compared to the calculations that do not include thermal coupling.

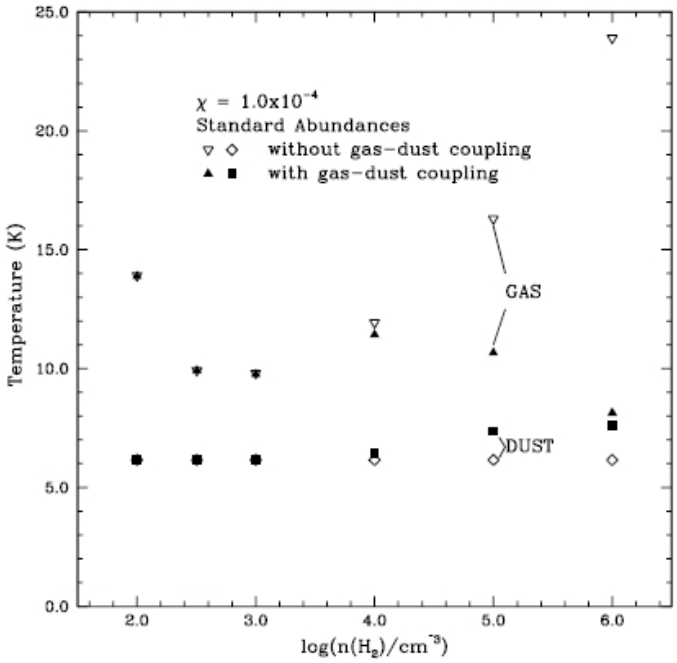

Abbildung 1: Dependence of the gas and dust temperatures on the density. The values were calculated with a radiative transfer model using standard abundances of molecular gas (10^{-5} - 10^{-8} relative to H_2) and dust (gas-to-dust ratio = 100 by mass) in molecular clouds. The ättenuation factor"χ gives the assumed fraction of dust-heating ISRF photons that reach the inner parts of the cloud used in this model. Open symbols show the evolution of the gas and dust temperatures when thermal coupling is not included. Above $n(H_2) \approx 10^4$ cm^{-3} the effect of the thermal coupling (filled symbols) becomes evident. Instead of diverging in the case without coupling, the gas and dust temperatures converge until they become almost equal at $n(H_2) \approx 10^6$ cm^{-3}. (Figure taken from Goldsmith 2001.)

3 Ammonia in molecular clouds

Ammonia (NH_3) is one of the most important molecules in the study of molecular clouds. It has a large number of transitions that are collisionally excited only at densities above $n(H_2) \approx 10^3$ cm^{-3} (see Sec. 4.2) which is the reason why NH_3 is commonly used as a tracer of dense regions in molecular clouds (Seo et al. 2015). The relative populations of the dipole transitions (for example the rotation states (1,1) and (2,2)) depend only on collisions with H_2 and therefore allow a direct measure of the gas kinetic temperature. A comparison of the brightness temperatures of the observed NH_3(1,1) and NH_3(2,2) lines can be used to determine the kinetic temperature of the gas. This method, that depends on the unique quantum structure of the ammonia molecule, has the advantage that the determined kinetic temperature is independent of turbulent motions of the observed gas (Juvela et al. 2012). In comparison to NH_3 the utility of other molecules is limited because temperature measurements from other molecules use the broadening of emission lines and it is difficult to separate the effects of the turbulent gas motions from the thermal effect on the broadening. Because of these properties emission from NH_3 is a good tool to measure the gas temperatures in the densest regions of molecular clouds.

4 Density estimations in molecular clouds

The thermal balance calculations described in Section 2 show that thermal coupling is expected to become relevant at densities above $n(H_2) \approx 10^4$ cm^{-3}. Observational investigations of the thermal coupling must therefore be restricted to the densest regions in molecular clouds, the cloud cores. Several independent arguments suggest that the densities in these regions are high

enough to allow a coupling of gas and dust temperatures. Since observations of ammonia will be used for the actual comparison of gas and dust temperatures in Sectin 6, the following density estimations are based on NH_3 observations.

4.1 Chemical argument

Since ammonia is frequently observed in molecular clouds there must be a reliable chemical process that produces the observed amounts of the molecule. An important reactor in this formation process is N_2H^+. This ion is in turn destroyed by CO and is therefore not available for the formation of NH_3 in regions where CO is abundant. The formation of ammonia from N_2H^+ is therefore only possible in regions where CO is depleted by freezing-out onto dust grains. Depletion of CO and therefore the formation of ammonia needs densities of $n(H_2) \geq 10^4$ cm^{-3} (Bergin & Tafalla 2007).

4.2 Critical density for molecular line emission

Spontaneous transmission from higher to lower energy levels in a molecule lead to emission of a photon with a frequency that is set by the energy difference between the two levels. This spontaneous transmission happens with a certain probability and the associated photon emission rate can be measured. If there is no external process that excites the molecules from the lower energy levels back to the higher levels, after a given time most of the molecules will have had a transition from the higher to the lower level and the emission of photons stops. In a molecular cloud this means that the spectral line associated with that transmission is not detected if there is no continuous excitation process. At the low temperatures in molecular clouds all other excitation processes other than collisions with other molecules can be neglected. Because H_2 is the most abundant molecule, collisions of any molecule in a cloud will most probably happen with a H_2 molecule. If the

collision rate between a molecule and H_2 is at least equal to the rate at which a molecule deexcites spontaneously by emission of a photon, molecules will continuously get excited after emitting. This leads to continuous emission and the emitting molecule can be detected. The density of H_2 at which this equilibrium begins to hold is called critical density. This threshold density gives a lower limit that has to be reached for continuous emission and is different for every molecule and transition line.
The critical density n_{crit} (of hydrogen molecules) can be calculated as

$$n_{crit} = \frac{A}{\sigma \overline{v}_{\mathrm{H_2}}} \tag{3}$$

where A is the Einstein coefficient for the considered transition (this is the rate at which a spontaneous transition from a higher to lower energy level happens on average), σ is the collision cross-section of the molecule, for which the critical density is wanted (e.g. $\sigma \approx 10^{-15}$ cm^2 for NH_3, Ho & Townes (1983)). In molecular gas with a certain temperature T the velocities of the individual H_2 molecules vary according to a Maxwell-distribution and then the average velocity $\overline{v}_{\mathrm{H_2}}$ of the H_2 molecules is given by:

$$\overline{v}_{\mathrm{H_2}} = \sqrt{\frac{3kT}{m_{\mathrm{H_2}}}} \tag{4}$$

k is Boltzmann's constant and $m_{\mathrm{H_2}}$ the mass of a hydrogen molecule. The term in the denominator of the Equation (3) is then the rate at which in a certain volume collisions of one H_2 particle with another molecule happen on average. For the inversion transitions (1,1) and (2,2) of the ammonia molecule the Einstein coefficients A are in the order of 10^{-7} s^{-1} for both transitions (Ho & Townes 1983). The result is a critical H_2 density of $n_{crit} \approx 10^3$ cm^{-3} for these ammonia transitions. This value lies an order of magnitude below the threshold density for the formation of NH_3 in molecular clouds (see Sect.

4.1) which means that the critical density for NH_3(1,1) and NH_3(2,2) line emission is reached wherever ammonia is present. This also implies that the entire ammonia content in molecular clouds is emitting in the NH_3(1,1) and NH_3(2,2) line.

The fact that n_{crit} only gives a lower limit for the density in molecular clouds becomes evident when one compares the critical densities for NH_3 and N_2H^+ emission. Johnstone et al. (2010) found that in most cores in Perseus that show emission in NH_3 the N_2H^+(1-0) line can also be detected. The critical density of this N_2H^+ line is about two orders of magnituede larger than for the above mentioned ammonia lines ($n_{crit}(N_2H^+) \approx 10^5 cm^{-3}$, Ungerechts et al. (1997)) which means that in most Perseus cores in which ammonia is detected, the density lies two orders of magnitude above the critical density for ammonia emission.

4.3 Estimation of volume densities from surface densities by assuming spherical symmetry

Contrary to volume densities, the projected surface densities of molecular cloud cores can be directly measured. If the cores are assumed to be on average of spherical shape and that the densities are uniform across a core then the volume density n can be estimated from the surface density Σ by the simple relation

$$n \approx \frac{3}{4}\frac{\Sigma}{R} \tag{5}$$

where R is the radius of the spherical cloud core (the factor $3/4 \cdot R$ arises from dividing the area of the projected surface of the cloud core by its volume). Rosolowsky et al. (2008) find that the typical NH_3 surface density in Perseus cores is $\Sigma(NH_3) \approx 3 \cdot 10^{14}$ cm^{-2}. The relative abundance of H_2 to NH_3 is approximately 10^8 (Goldsmith 2001), resulting in a total typical surface

density of $n(H_2) \approx 3 \cdot 10^{22}$ cm^{-2} (other molecules than H_2 can be neglected because of their low relative abundances). The mean size of cores in Perseus, derived from measurements of ammonia emission regions, is $R \approx 0.09$ pc (Rosolowsky et al. 2008 ; Jijina et al. 1999). With Equation (5) the average volume density in cloud cores in Perseus can then be estimated as

$$n(H_2) \approx \frac{3}{4} \quad \frac{10^8 \cdot 3 \cdot 10^{14} cm^{-2}}{2.8 \cdot 10^{17} cm} \approx 10^5 cm^{-3} \tag{6}$$

All three methods described in this section show that the density that is theoretically required for thermal coupling is reached in ammonia cloud cores. Observations of such cores are therefore expected to show that the gas and dust temperatures there are similar (within ≈ 5 K) and approach each other at the highest densities.

5 Measuring gas and dust temperatures

Investigating the thermal coupling in molecular clouds requires separate measurements of the gas and dust temperatures in the dense cloud cores. The following sections describe how gas and dust temperatures are measured in the specific case of the Perseus molecular cloud. Here, the gas temperatures were measured from ammonia spectra by Rosolowsky et al. (2008) and the thermal FIR emission from the dust was used to determine the *effective* dust temperatures by Zari et al. (2016). The suitability of those methods for the direct comparison of the gas and dust temperatures will also be discussed below.

5.1 Gas kinetic temperatures from ammonia line observations

It is possible to calculate the kinetic temperature from the ratio between the intensities of the main and hyperfine components of the NH_3(1,1) line and the ratio between the intensites of the NH_3(1,1) and NH_3(2,2) line. Generally, the measured flux density of a spectral line (in radio astronomy usually expressed as an antenna temperature T_a) can be expressed in terms of the line excitation temperature T_{ex} and the optical depth τ. For example for the (1,1) transition line of ammonia:

$$T_a(1,1) = \eta_{mb}\eta_f \left[T_{ex}(1,1) - T_{bg}\right] \left(1 - e^{-\tau(1,1)}\right) \tag{7}$$

where η_{mb} and η_f are the main beam efficiency of the antenna respectively the filling fraction of the source in the antenna beam and $T_{bg} = 2.75$ K is the universal background temperature. Using this expression and assuming equal excitation temperatures for the ammonia (1,1) and (2,2) emission lines as well as equal beam efficiency and filling fractions, the ratio between $T_a(1,1)$ and $T_a(2,2)$ can be written as

$$\frac{T_a(1,1)}{T_a(2,2)} = \frac{1 - e^{-\tau(1,1)}}{1 - e^{-\tau(2,2)}} \tag{8}$$

By using the same assumptions, the optical depth of an emission line can be calculated from the ratio between the main and satellite components of the line (indicated as m and s). The satellite components arise because of the hyperfine splitting of the emission line induced by the electric field of the electrons in the NH_3 molecule. While the satellite components of the (2,2) line are too weak to be detected, the optical depth $\tau(1,1)$ can be directly calculated from the ratio between the main and satellite components of the (1,1) line:

$$\frac{T_a(1,1,m)}{T_a(1,1,s)} = \frac{1 - e^{-\tau(1,1,m)}}{1 - e^{-a\tau(1,1,m)}} \tag{9}$$

Here a is the ratio between the intensity of the hyperfine component and the main component ($a = 0.28$). If one then solves Equation (8) for $\tau_a(2,2)$:

$$\tau_a(2,2) = -\ln\left\{1 - \frac{T_a(1,1)}{T_a(2,2)} \cdot \left[1 - e^{-\tau(1,1)}\right]\right\} \tag{10}$$

and combines Equation (9) and (10), the ratio between $\tau(1,1)$ and $\tau(2,2)$ is known.

This ratio can be expressed in a different way by using the definition of the optical depth (Rosolowsky et al. 2008):

$$\frac{\tau(1,1)}{\tau(2,2)} = \left[\frac{\nu(1,1)}{\nu(2,2)}\right]^2 \frac{\Delta\nu(1,1)}{\Delta\nu(2,2)} \frac{T_{ex}(1,1)}{T_{ex}(2,2)} \frac{|\mu(2,2)|^2}{|\mu(1,1)|^2} \cdot \frac{g(2,2)}{g(1,1)} \cdot \exp(-\frac{T_0}{T_R}) \tag{11}$$

Here the *rotation* temperature T_R describes the number of molecules that undergo the (1,1) transition relative to the number that undergo the (2,2) transition. The energy gap between these two states, expressed in K, is T_0 = 41.5 K (Ho et al. 1979). The values of the rest frequencies ν, dipole matrix elements ($|\mu(1,1)|^2, |\mu(2,2)|^2$) and the statistical weights g of the two transitions are known and by assuming equal line widths $\Delta\nu$ and excitation temperatures T_{ex} , Equation (11) can be simplified to:

$$\frac{\tau(1,1)}{\tau(2,2)} = \left[\frac{\nu(1,1)}{\nu(2,2)}\right]^2 \frac{20}{9} \exp\left(-\frac{T_0}{T_R}\right) \tag{12}$$

The rotation temperature T_R can be related to the kinetic gas temperature T_k by using detailed balance arguments (Swift et al. 2005):

$$T_R = T_k \left\{ 1 + \frac{T_k}{T_0} \cdot \ln \left[1 + 0.6 \exp \left(-\frac{15.7}{T_k} \right) \right] \right\}^{-1} \tag{13}$$

By combining Equations (9), (10), (12) and (13) it is possible to calculate the kinetic temperature from the ratios between the intensity of the main and hyperfine components of the NH_3(1,1) line and the ratio between the intensites of the NH_3(1,1) and NH_3(2,2) line.

5.2 Effective dust temperatures

When a photon is absorbed by a solid body, such as a dust grain, its energy is evenly distributed among the numerous vibrational energy states of the atoms and molecules that make up the dust grain. Transitions between the different energy states lead to the emission of photons at all frequencies. The temperature T of a grain is defined by the frequency ν_{max} at which the intensity of the emission has a maximum, as described by Wien's displacement law (here given in the frequency dependent form):

$$\nu_{max} \propto T \tag{14}$$

The intensity of this thermal emission at the frequency ν of a body at temperature T is described by Planck's law

$$B_\nu(T) = \frac{2h\nu^3}{c^2} \frac{1}{e^{h\nu/kT} - 1} \tag{15}$$

where $B_\nu(T)$ is the intensity of the radiation, h is the Planck constant, k is Boltzmann's constant and c is the speed of light. The index ν indicates the frequency dependency of the intensity. Bodies whose emission show an intensity distribution like that are called *blackbodies*. The maximum of the

dust emission in molecular clouds lie in the far infrared (FIR), corresponding to dust temperatures of $\approx$ 10 - 100 K. Sub-mm wavelengths are therefore frequently used to observe the dust content of clouds and to measure the dust temperatures.

Equation (15) describes the thermal radiation from a single dust grain but when observing a molecular cloud one will always detect radiation from a dust column along the line of sight. One consequence of this is that emission from dust grains at the interior of a cloud will partly be absorbed by dust grains in the outer parts of the cloud and therefore the intensity distribution of the overall dust emission will be different from the emission of just a single particle. Solving the radiative transfer equation for a dust cloud that is both emitting and self-absorbing leads to the intensity distribution of a so called *modified* blackbody:

$$I_\nu(T) = B_\nu(T)(1 - e^{-\tau_\nu}) \tag{16}$$

The optical depth τ_ν depends on the absorption cross section of the dust grains and gas particles in the molecular cloud. Because this cross section is small for FIR radiation molecular clouds are optically thin for dust emission ($\tau_\nu \ll 1$). The temperature of a modified blackbody can be calculated by determining the frequency ν_{max} where the intensity has a maximum and then using Wien's displacement law. In reality it is inefficient to measure ν_{max} directly from the shape of the intensity distribution, because this would require spectroscopy that covers a wide frequency range. Therefore, to measure the temperature of a large number of sources, the intensity at only a small number of frequencies is measured and then a model modified blackbody is fitted to the data.

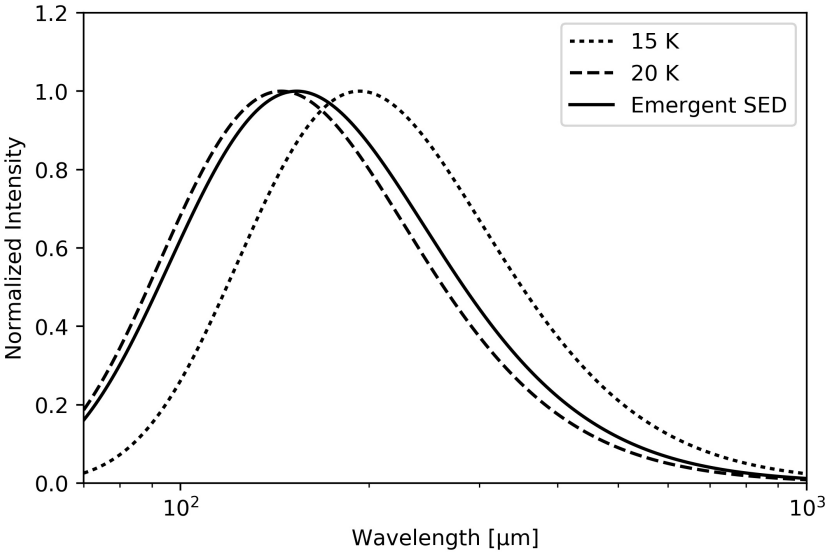

Abbildung 2: Normalized SEDs of two modified blackbodies at different temperatures. The solid line shows the emergent SED (also a modified blackbody) when the two different blackbodies are summed up. Note that the intensities are normalized here for the sake of comparison of the positions of the maxima. The actual maximal intensity of the 20 K blackbody is about five times larger than the maximal intensity of the 15 K blackbody. Therefore the emergent SED is domintated by the warmer blackbody (see also text for explanation). Optical depths τ_ν are the same for both blackbodies.

As mentioned earlier, when observing dust the detector will collect photons from every dust grain along the line of sight. Because of that not only the dust grains in the dense cloud cores are detected but also dust located in the outer layers of the observed molecular cloud. If there is a temperature gradient along the line of sight, caused for example by an embedded protostar in a cloud core or heating by massive stars inside the molecular cloud complex, the resulting spectral energy distribution is a superposition of the theoretical modified blackbodies of dust at different temperatures (see Figure

2). At low temperatures, a small increase of T produces a large increase of intensity and as a result most of the detected photons will be emitted from warmer regions along the line of sight. This effect is non-linear and therefore the measured dust temperature is not a simple average of the dust temperatures along the line of sight, but is biased high by the warmer dust layers (Shetty et al. 2009). What is more is that the ISRF photons that heat the dust grains in molecular clouds do not have the same effect on every grain. The temperatures of grains heated by an external radiation field depend for example on the dust composition and size, where larger grains have typically lower temperatures (Krügel & Walmsley 1984). The temperatures that are determined by using the method described above are therefore interpreted as *effective* temperatures for a dust column along the line of sight (Lombardi et al. 2014) and do not necessarily provide a physical description of the properties of dust grains inside molecular cloud cores.

6 Gas and dust temperatures in Perseus

6.1 The Perseus molecular cloud

Perseus is one of the best studied nearby molecular clouds. Its most active star formation regions, the clusters IC348 and NGC1333 contain numerous young stars with spectral types B or later (Rebull et al. 2007). The relatively low number of massive stars (compared for example to Orion) and the lack of O-type stars make Perseus the typical example of an intermediate star formation region. Young stellar objects (YSOs) are also found outside of IC348 and NGC1333, mostly concentrated in the dense regions B1 and L1455 (Young et al. 2015). Commonly used distance estimations lie within 230 - 260 pc (e.g. Zari et al. 2016; Rosolowsky et al. 2008) while some estimations reach

out up to 350 pc (Schlafly et al. 2014). In addition to point sources (YSOs), Perseus has been extensively studied in extended emission from molecular gas and dust, making it a suitable region for the comparison of gas and dust temperatures.

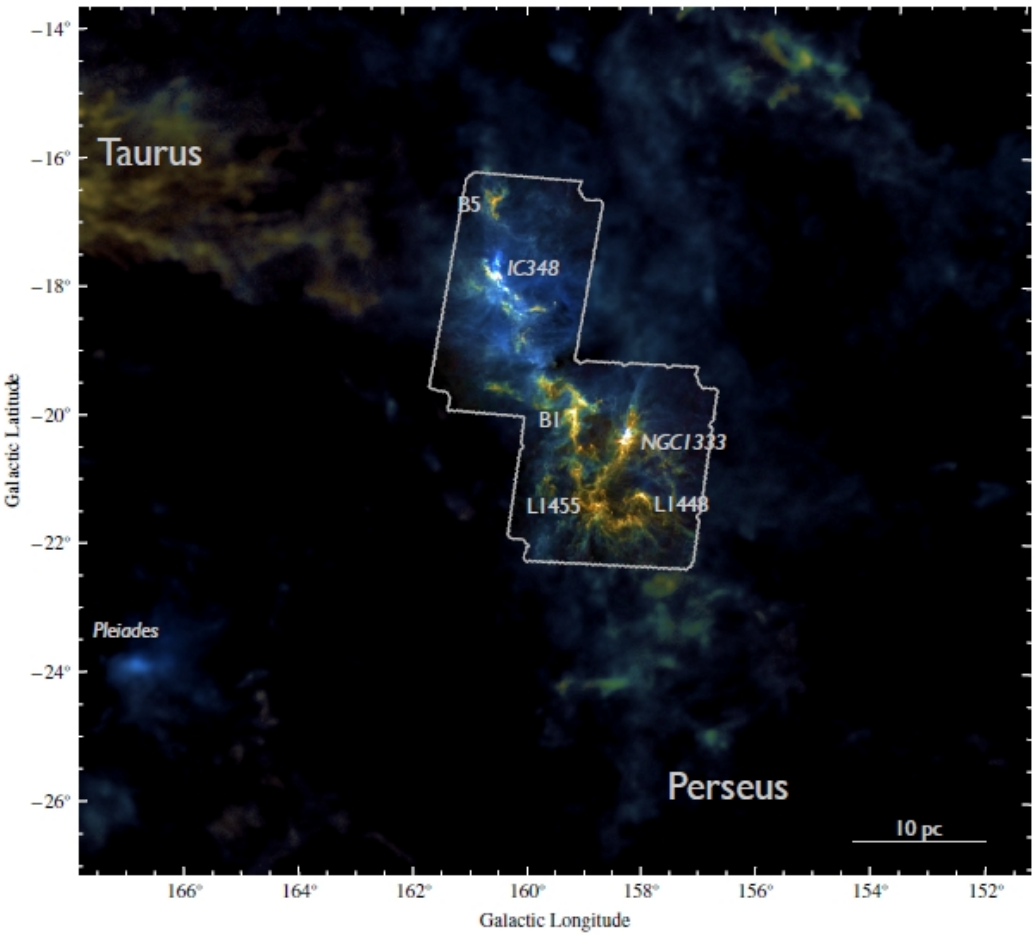

Abbildung 3: Three color dust emission map of Perseus. The intensities in the 250 µm (blue), 350 µm (green) and 500 µm (red) bands were measured with the *Herschel* and *Plank* space observatories. Labels show prominent star formation regions inside the cloud, including the two clusters IC348 and NGC1333 and other dense regions. (Figure taken from Zari et al. 2016.)

6.2 Ammonia gas kinetic temperatures in Perseus

In 2006, Rosolowsky et al. observed 192 dense cores and core candidates in the Perseus molecular cloud with the Robert F. Byrd Green Bank Telescope (GBT). Among other lines, they observed the NH_3(1,1) and NH_3(2,2) hyperfine transitions at frequencies near $\nu = 23$ GHz. A model spectrum was fitted to the entire spectrum of each observed cloud core, fitting all measured lines simultaneously. The least squares fit provided several physical parameters, including the gas kinetic temperature T_k (one value for each core), from which in a later step the NH_3 column density was calculated. In a number of sources, the NH_3(1,1) transition could be detected, but not the (2,2) line. Since the computation of the model spectra requires values for both of these lines, in those cases an upper limit was assumed for the NH_3(2,2) line and the resulting kinetic temperature is also an upper limit (see Sect. 5.1). Having only an upper limit for T_k, the calculated column density for these sources is a lower limit. The gas temperatures in the 192 cloud cores span a range from a minimum of $T_k = 9.05$ K up to $T_k = 26$ K in the warmest core, while the NH_3 column densities vary by three orders of magnitude, from $\Sigma(NH_3) = 5.5 \cdot 10^{12}$ cm^{-2} to $\Sigma(NH_3) = 1.3 \cdot 10^{15}$ cm^{-2}. If there is a linear relationship between the column densities (= surface densities) and the overall volume densities n(H_2) as assumed in Section 4.3, the volume densities in the cloud cores also vary within three orders of magnitude. It is therefore not expected that the effects of thermal coupling will be of the same significance in all of the 192 observed cores.

6.3 Dust effective temperatures in Perseus

Zari et al. (2016) used the modified blackbody model described in Section 5.2 to create a dust effective temperature map of Perseus from observations by the Herschel and Plank space observatories. The bandwidths of the filters used with the Herschel imaging camera PACS and the Plank bolometers

(SPIRE) are too large to measure the distribution of the specific intensity directly. Figure 4 shows the frequency range and relative throughput of the used PACS (70, 100 and 160 µm) and SPIRE (250, 350, 500 µm) bands. The PACS 70 µm band was not used because observations in this band showed very low flux and emission from molecular clouds at such short wavelenghts is not always optically thin because the dust particles absorb more effectively at shorter wavelengths.

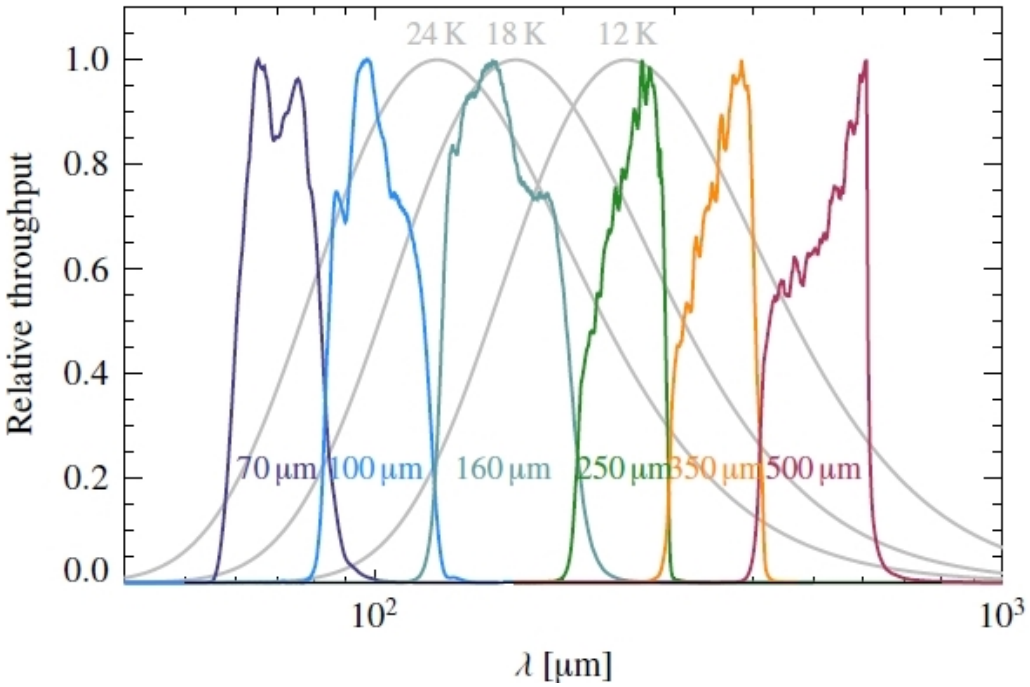

Abbildung 4: Throughputs of the six PACS and SPIRE filters in color. Gray graphs show the normalized SEDs of three modified blackbodies with the same optical depth τ_ν and different temperatures. The maximum of the 12 K modiefied blackbody for example lies within the 250 µm band while the flanks can be sampled by the 160 µm respectively 350 and 500 µm filter bands. (Figure taken from Zari et al. 2016)

The PACS and SPIRE instruments measure the total flux integrated over the bandwidth of a filter. As a result, the distribution of the specific intensity of the dust radiation is sampled by only five datapoints, one for each filter band. A fitting procedure is therefore necessary to determine the shape of the modified blackbody from the observations. The input for this fit is a model modified blackbody spectrum with parameters T and τ_ν and the response of the detectors to this model spectrum is simulated. In the next step the input parameters are modified until there is a good match between the observed and theoretical fluxes. This procedure is repeated for every pixel of the Herschel-Plank observations of Perseus and the result is a map of effective dust temperatures with distinct values for each pixel (Figure 5). This temperature map was used to determine the dust effective temperature at the central positions of the 192 cloud cores that Rosolowsky et al. (2008) observed in Perseus.

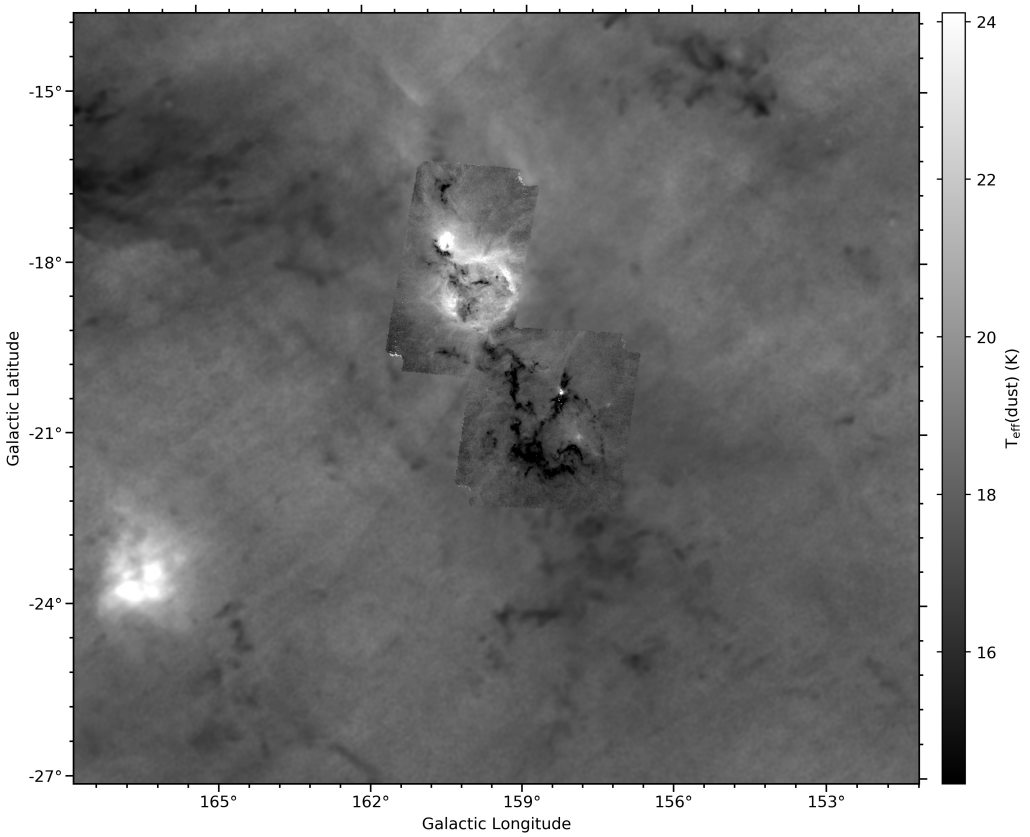

Abbildung 5: Dust effective temperature map of Perseus. Lighter shading indicates higher temperatures.

6.4 Comparing gas kinetic and dust effective temperatures

The fundamental difference in the methods to determine the gas and dust temperatures in molecular clouds has to be considered when they are used to evaluate the theoretically predicted thermal coupling. Observations of ammonia spectral lines provide a thermodynamic defined kinetic temperature of the gas. It is restricted only to the densest regions inside molecular cloud cores because there is essentially no other ammonia along the line of sight. The

measured dust temperatures are affected by line-of-sight effects: Not only the dust in the dense cores is measured but every dust grain between the cores and the observer contributes to the measured dust temperature. If there are large temperature gradients along the line of sight, this effective temperature therefore does not necessarily reflect the actual dust temperatures inside the cloud cores.

Figure 6 shows the measured ammonia temperatures and dust effective temperatures of 153 cores in Perseus. For a number of cores the gas temperatures could not be well determined and only an upper limit could be calculated by Rosolowsky et al. (2008) (blue subsample). Due to this uncertainty those cores are not considered in the further analysis of the data.

The 116 cores with well determined ammonia temperatures (green) show a correlation between gas and effective dust temperatures. While there are some cores with very low gas temperatures ($\approx$ 9 K) that have effective dust temperatures of over 15 K, the overall trend is that gas temperatures are rising with increasing effective temperatures. In most cores the gas temperature is lower than the effective dust temperature. This is in agreement with the results found by Forbrich et al. (2014) for cloud cores in the Pipe Nebula. Above temperatures of 20 K the temperature correlation breaks down and the gas and effective dust temperatures appear to be independent. The circumstance that the measured dust effective temperatures can be strongly affected by dust temperature gradients along the line of sight (see Sec. 5.2) suggests that considering special environments and internal properties of the cores is important when comparing gas and effective dust temperatures.

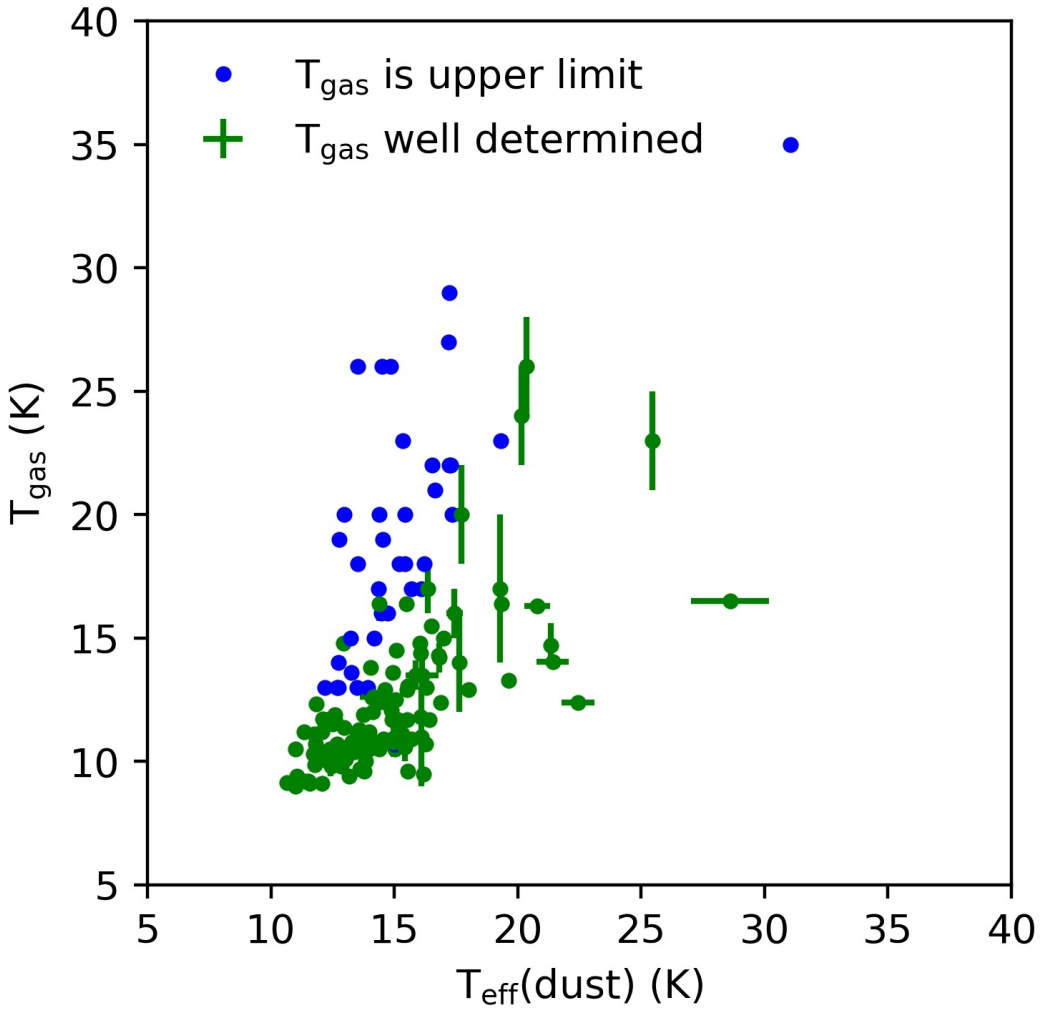

Abbildung 6: Comparison of kinetic gas temperature and effective dust temperature in Perseus cores. The gas temperatures of the blue subsample represent upper limits. While all cores in the green subsample have given errors in gas and dust effective temperatures, errorbars are only displayed when the error exceeds 0.5 K for reasons of clarity (see Appendix A for a full list of core temperatures and errors).

To study the influence of environmental effects the cloud cores are divided by the region in Perseus in which they are located. The three regions considered here are the two clusters NGC1333 and IC348 and the more quiescent rest of the molecular cloud. The borders of these regions were defined by Rebull et al. (2007).

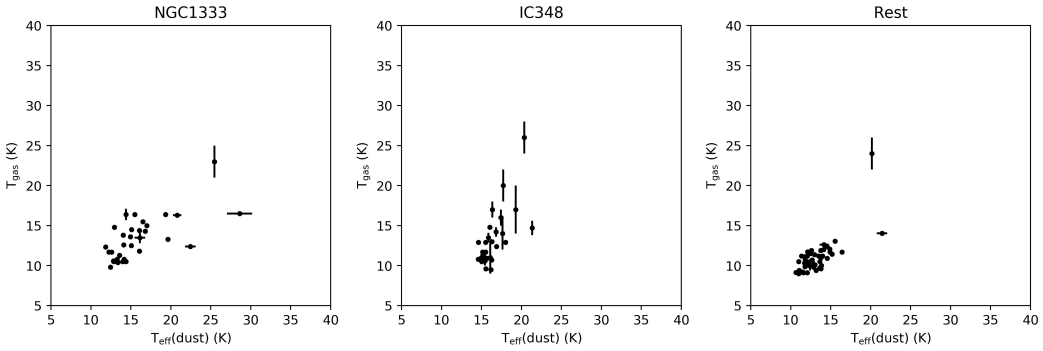

Abbildung 7: Comparison of gas temperatures an dust effective temperatures of cores located in the clusters NGC1333 and IC348 and the rest of the Perseus molecular cloud. Errorbars are displayed when the error is larger than 0.5 K.

The cores which are located in neither of the two clusters of Perseus (right panel in Figure 7) have on average the lowest gas and dust temperatures and span the smallest temperature ranges. Apart from two outliers that show a large difference between measured gas and dust temperatures, all cores lie within a region between gas temperatures from 9 - 14 K and dust temperatures from 11 - 16.5 K. There is a correlation between T_{gas} and T_{dust} and above dust temperatures of 15 K there are no cores with gas temperatures lower than 11 K.

Above gas temperatures of about 12 K the effective dust temperature is independent of the gas temperature in cores in NGC1333 (left panel in Figure 7). There is a bulk of cores with low gas and dust temperatures but above

gas temperatures of approximately 12 K the effective dust temperature is independent of the gas temperature. Except for one core the gas temperature never rises above 17 K while the dust effective temperatures span a range from $\approx$ 11.8 K to 28.6 K. NGC1333 is a young star forming region containing numerous embedded pre-main-sequence stars, Herbig-Haro objects and molecular outflows and jets (Lada et al. 1996). It can therefore be expected that the measured effective temperatures are strongly affected by the temperature gradients present in such an environment.

In comparison with NGC1333 there are no low dust temperatures measured in IC348 cores. The lowest measured dust temperature is about 14 K while gas temperature in those cores scatter around 10 K by 1 - 2 K. The correlation between gas and dust temperatures in better in IC348 than in NGC1333. There are no extreme high values of dust effective temperatures relative to gas temperatures in IC348 cores. This is somewhat surprising because the star formation activity in both clusters is similar and therefore similar temperature gradient effects on the effective dust temperature would be expected. Instead, in IC348 there are more cores with high gas temperatures compared to NGC1333. The mean dust effective temperature of cores that are located in one of the two clusters is 16.1 K. This value is 3 K higher than then mean dust effective temperature of cores in the rest of Perseus.

Embedded young stellar objects (YSOs) in cloud cores can represent another source for temperature gradients that bias the measured dust temperatures high. Figure 8 compares the gas and dust temperatures of cores without YSOs (left panel) and cores with at least one embedded YSO (right panel) inside the GBT beam that was used to measure the NH_3 emission lines ($31''$ from the pointing center respectively 0.04 pc at the assumed distance of Perseus of 260 pc). The positions of the YSOs were taken from Young et al. (2015).

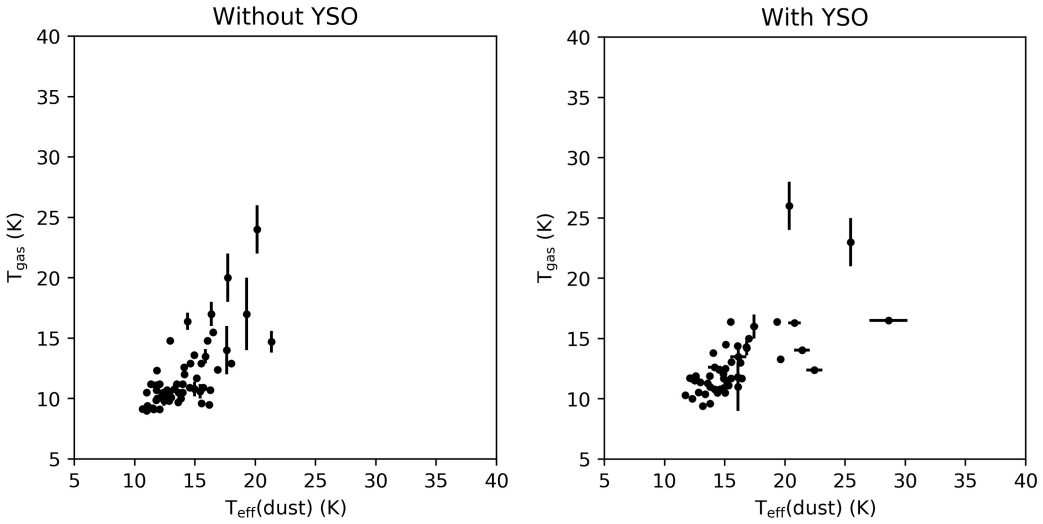

Abbildung 8: Gas and dust effective temperatures of cores that contain no embedded source (left) and cores that contain at least one YSO within the central 31″.

At low temperatures the cores containing embedded YSOs show a similar temperature distribution than the ones without a YSO. The average dust effective temperature is rising with the gas temperature until at gas temperatures above 13 K there is a sudden increase of very high dust temperatures in the cores that contain a YSO. Six of the eight cores with dust effective temperatures over 20 K contain an embedded source and the warmest of them are additionally located in NGC1333.

The fact that most of the cores with high T_{dust} lie both in the active environment of the NGC1333 cluster and also contain a YSO makes it hard to determine whether the cluster environment or the embedded source is the main reason for a high dust effective temperature. A comparison of the total number of cores in Perseus that contain a YSO (*With YSO*) with the subsample of cores that is located in neither of the two clusters (*Rest*) suggests the YSOs are not the main reason for high dust effective temperatures. Of

the 55 cores in the *Rest* subsample 21 contain an embedded source but only two cores have $T_{dust} > 20$ K (both of them contain at least one YSO). The the mean dust effective temperature of these 21 cores is approximately 13.8 K which is similar to the mean dust temperature of the remaining 34 cores which do not contain an embedded source (12.7 K). Therefore it appears plausible that the environmental effects and temperature gradients within a cluster have a larger effect on the measured dust effective temperatures than an embedded YSO.

6.5 Thermal coupling: Temperature difference vs. density

One of the effects of thermal coupling is that it determines the behavior of gas kinetic temperatures at high densities. Therefore, in analogy to Figure 1, here the ammonia gas kinetic temperatures and dust effective tempeatures in the Perseus cloud cores are plotted against the density which was calculated by using Equation (6). At low densities the average gas temperature is about 20 K and drops to values between 9 and 17 K in the density range from 10^4 to $2 \cdot 10^5$ cm^{-3}. At higher densities there are no cores with T_k greater than 13 K, but cores with the coldest temperatures of about 10 K are already found at low densities of 10^4 cm^{-3}. The low gas temperatures even at high densities are confirming the prediction by Goldsmith (2001) that the gas is thermally coupled to the dust at high densities. Without the coupling the gas temperature is expected to be consistently rising above densities of about 10^4 cm^{-3} (see Section 2.4).

The dust effective temperature behaves similar as the gas temperature in that it drops from high temperatures of over 20 K at low densities to lower temperatures as the density increases. While the average effective temperature drops, there is still considerable scatter even at high densities. Five of the cores with $T_{dust} > 19$ K at densities larger than 10^4 cm^{-3} are located in NGC1333. Their effective dust temperatures are therefore expected to be

biased high by environmental effects. Above densities of $2 \cdot 10^5$ cm^{-3} all of the observed cores have dust effective temperatures lower than 15 K and are colder than 13 K at the highest densities. However, there is already a number of cores with dust effective temperatures colder than 13 K at densities lower than 10^5 cm^{-3}.

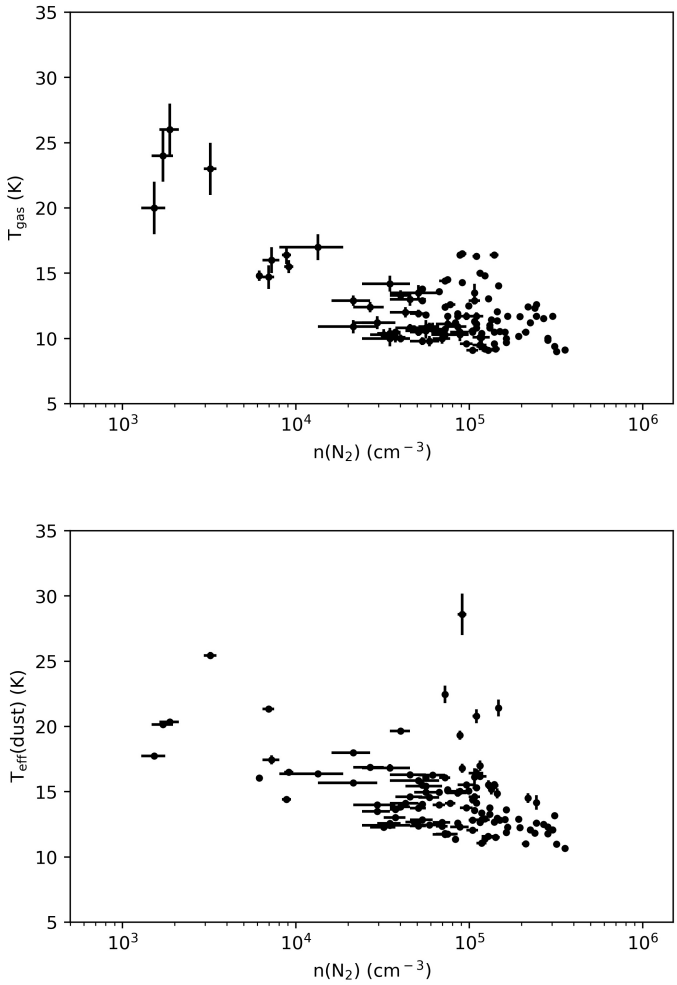

Abbildung 9: Gas kinetic temperatures (top) and dust effective temperatures (bottom) relative to H_2 denstiy. The density-axes are on a logarithmic scale.

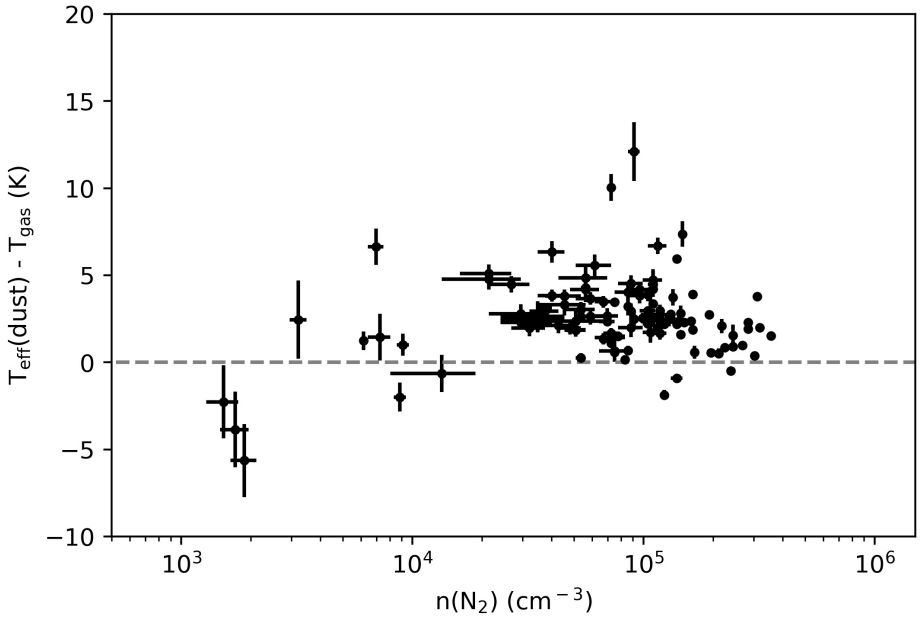

Abbildung 10: Difference between dust and gas temperatures in Perseus cloud cores relative to H_2 volume density (calculated from ammonia column densities using Eq.(4) and r = 0.09 pc). The dashed grey line represents equal gas and dust effective temperature.

Figure 10 shows the difference between gas and effective dust temperatures depending on the density in the 116 cores for which the gas temperatures are well determined (see green subsample in Fig. 6). As seen before the dust effective temperature is larger than the gas temperature for the majority of the cores ($T_{dust} - T_k > 0$). There is a large scatter of about 10 K around 0 K in temperature difference up to densities of n(H_2) $\approx 10^4$ cm^{-3} that reduces at higher densities. Again, there is a large temperature difference in a number of cores (with n(H_2) $\approx 10^5$ cm^{-3}) located in NGC1333 where the dust effective

temperature is up to 10 K larger than the gas temperature. As predicted by the thermal balance calculations that include thermal coupling the gas and dust temperatures lie within 5 K in cores where the density is larger than $\approx 10^5$ cm^{-3} instead of diverging at high densities. There are some cores within a large density range in which the gas and dust effective temperature are essentially equal. This temperature equality is not necessarily caused by thermal coupling but due to the general scatter in measured gas and dust effective temperatures at intermediate densities. The temperatures in the densest cores measured in Perseus lie within 5 K but their densities are almost one order of magnitude smaller than the density of $n(\mathrm{H_2}) \approx 10^6$ cm^{-3} that is theoretically required for the temperatures to be equal due to thermal coupling.

6.6 Linear fits

The figures in Section 6.4 show that there is a linear correlation between the gas temperature and the dust effective temperature as can be expected when the gas and dust in a cloud core are thermally coupled. To quantitatively describe this correlation a linear orthogonal distance regression (ODR) was performed on the six subsamples of Perseus cores. This regression method takes the errors in both variables into account. Since most of the outliers with relatively high gas kinetic and/or dust effective gas temperatures appear to have large errors, the ODR automatically minimizes the influence of the outliers on the fit. The linear fits shown in Figure 11 are of the form

$$T_{gas} = k \cdot T_{eff}(dust) + d \tag{17}$$

where the fit parameters k and d describe the slope and the intercept on the T_{gas} axis of the fit line. At first sight there appear to be two types of fits, one with a relatively steep slope resulting from the cluster subsamples

(*IC348* and *NGC1333*) and the YSO subsample and a shallower type computed from the total Perseus sample (T_{gas} *well determined*), the sample of cores without YSOs and the cores that are not located inside one of the two clusters (*Rest*). The values of the fit parameters and their corresponding errors (1σ) are listed in Table 1.

Sample	**k**	δ**k**	**d**	δ**d**
T_{gas} well determined	0.84	0.08	0.03	1.07
IC348	1.50	0.39	-11.93	6.06
NGC1333	1.16	0.23	-3.67	3.18
Rest	0.79	0.11	0.49	1.35
Without YSO	0.56	0.10	3.44	1.26
With YSO	1.12	0.18	-3.69	2.51

Tabelle 1: Fit parameters resulting form a linear ODR-fit performed on the subsamples of Persues cores defined in Section 6.4. The parameters are defined in Eq. (17) and their standard errors are given as δk and δd.

The before mentioned ßteepfits all have slopes $k > 1$ where the IC348 sample has the steepest fit line with $k = 1.50$. The similarity of the fits to the YSO sample and the NGC1333 sample arises from the fact that 23 of the 33 measured cores in NGC1333 contain an embedded YSO. The samples *Rest* and *Without YSO* have the shallowest slopes. In addition to showing the shallowest slope, the fit to the *Without YSO* sample is also the only fit having an intersection d that is not negative or close to zero. A negative intersection on the T_{gas} axis means that the dust effective temperatures of the whole sample are shifted towards higher values than the gas temperatures (resulting in a *positive* intersection of the fit line on the T_{eff} axis). This is as expected because any present temperature gradients along the line of sight

will shift the measured dust temperatures to higher values, even if the gas and dust temperatures in the cloud cores were equal. Therefore it is surprising that in the cores that do not contain a YSO the intersection on the T_{gas} axis is negative. Environmental effects as a cause for this behavior can be excluded because the cores in this sample are located all over the Perseus molecular cloud, both in active and more quiescent regions. There is a number of cores that do not contain a YSO with very low gas temperatures but relatively large dust effective temperatures. This indicates that while the measured dust effective temperatures are relatively high because of environmental effects, the lack of heating by an embedded source keeps the gas temperatures low. This overabundance of cores with very low gas temperatures at high dust effective temperatures results in the shallow slope and and relatively large intersection d of the *Without YSO* fit.

All subsamples show a strong linear correlation between gas kinetic and dust effective temperatures (for all subsamples the Pearson correlation coefficient is r $\approx$ 0.7). Therefore, if for an observed sample of cloud cores only dust effective temperatures $T_{eff}(dust)$ are available, the corresponding gas kinetic temperatures can be estimated by using Equation (17) with the fit parameters listed in Table 1. If for example no information about the environment of the cloud cores is given, one can use the slope k and intersection d of the T_{gas} *well determined* fit to estimate the gas kinetic temperatures T_{gas} of the cores:

$$T_{gas}[K] = 0.84 \pm 0.08 \cdot T_{eff}(dust)[K] + 0.03 \pm 1.07[K] \tag{18}$$

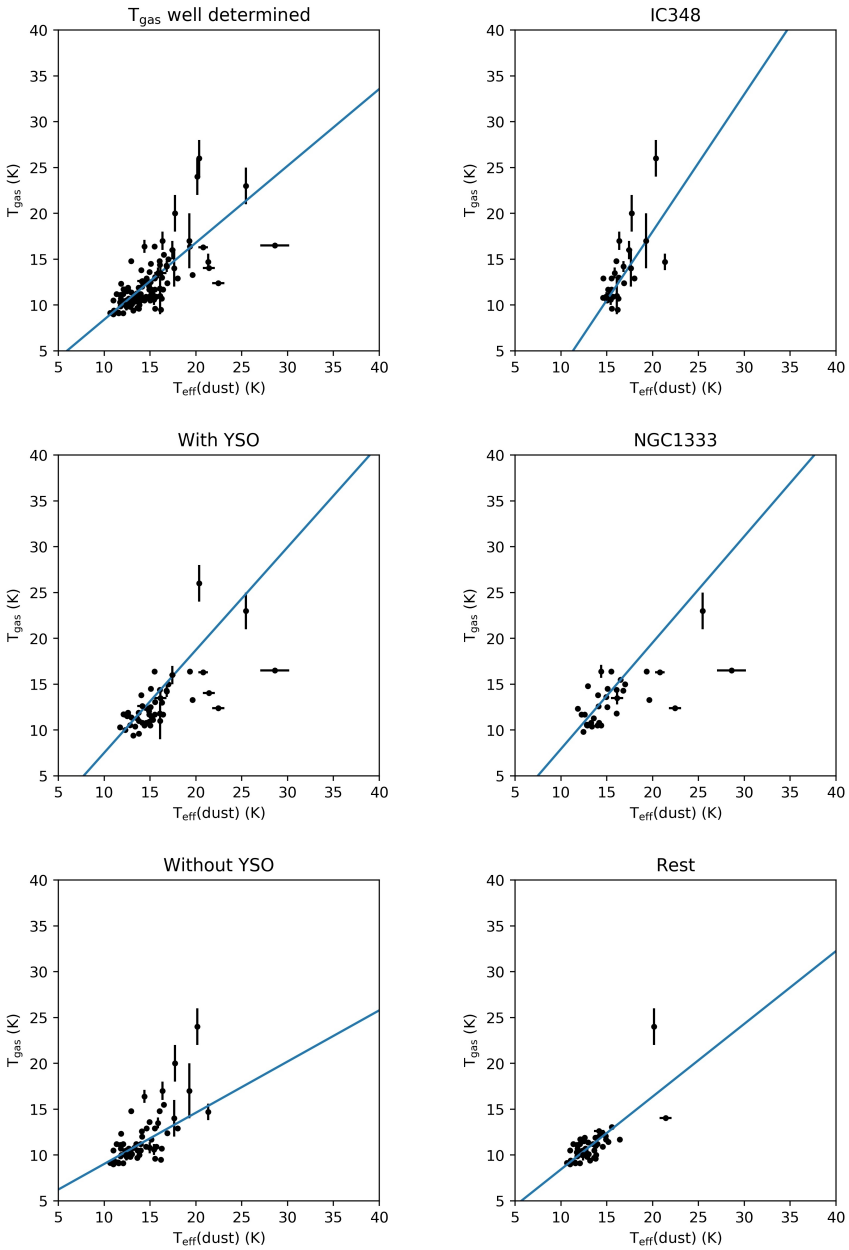

Abbildung 11: Linear ODR fits describing the correlation between the gas kinetic and dust effective temperatures in the different subsamples of Perseus cloud cores.

6.7 Conclusions

The main results found by investigating the cloud cores in Perseus can be summed up to:

- By comparing the gas kinetic and effective dust temperatures of cores in Perseus the general prediction of Goldsmith's thermal coupling model could be confirmed: The gas temperatures do not rise above densities of $n(H_2) \approx 10^4$ cm^{-3} but approach the dust temperatures until they lie within 5 K above densities of $n(H_2) \approx 10^5$ cm^{-3}. This means that the gas and dust in the densest cloud cores are thermally coupled.

- Dust temperature gradients along the line of sight, mainly caused by environmental effects in active regions within a molecular cloud, bias the measured dust effective temperature high. Embedded protostars within a cloud core do not have a considerable effect on the measured dust effective temperature.

- There is a strong linear correlation between the gas kinetic and dust effective temperature in cloud cores in Perseus. This correlation can be used to infer the gas temperatures from the dust effective temperatures but one should keep in mind that the temperature gradients present in cluster environments can lead to considerable scatter around this correlation. The safest prediction of the gas temperature can therefore be made from dust measurements of cores in more quiescent regions. Here in most cores the gas and dust effective temperatures lie within 3 K.

Aknowedgements: This research has made use of the VizieR catalogue access tool, CDS, Strasbourg, France. The original description of the VizieR service was published in A&AS 143, 23.

Literatur

Bergin, E. A. & Tafalla, M. (2007), ARA&A 45, 339.

Burke, J. R. & Hollenbach, D. J. (1983), ApJ 265, 223.

Forbrich, J. et al. (2014), A&A 568, 27.

Galli, D., Walmsley, M. & Gonçalves, J. (2002), A&A 394, 275.

Goldsmith, P. F. (2001), ApJ 557, 736.

Goldsmith, P. F. & Langer, W. D. (1978), ApJ 222, 881.

Gonçalves, J., Galli, D. & Walmsley, M. (2004), A&A 415, 617.

Ho, P. T. P. & Townes, C. H. (1983), ARA&A 21, 239.

Ho, P. T. P. et al. (1979), ApJ 234, 912.

Jijina, J., Myers, P. C. & Adams, F. C. (1999), ApJS 125, 161.

Johnstone, D. et al. (2010), ApJ 711, 655.

Juvela, M. et al. (2012), A&A 538, 133.

Krügel, E. & Walmsley, C. M. (1984), A&A 130, 5.

Lada, C. J., Alves, J. & Lada, E. A. (1996), AJ 111, 1964.

Lombardi, M. et al. (2014), A&A 566, 45.

Rebull, L. M. et al. (2007), ApJS 171, 447.

Rosolowsky, E. W. et al. (2008), ApJS 175, 509.

Schlafly, E. F. et al. (2014), ApJ 786, 29.

Seo, Y. M. et al. (2015), ApJ 805, 185.

Shetty, R. et al. (2009), ApJ 696, 2234.

Sipilä, O., Caselli, P. & Taquet, V. (2016), A&A 591, 9.

Swift, J. J., Welch, W. L. & Di Francesco, J. (2005), ApJ 620, 823.

Ungerechts, H. et al. (1997), ApJ 482, 245.

Young, K. E. et al. (2015), AJ 150, 40.

Zari, E. et al. (2016), A&A 587, 106.

Anhang A Physical properties of the cloud cores in Perseus

Table 2 lists the physical properties of the Perseus cloud cores. A description of the columns in given at the end of the table.

Tabelle 2: Properties of cloud cores in Perseus

ID	Region	RA	DEC	T_{gas} (K)	e_T_{gas} (K)	T_{eff} (K)	e_T_{eff} (K)	$\Sigma(NH_3)$ (10^{13} cm^{-2})	$e\_\Sigma(NH_3)$ (10^{13} cm^{-2})	$n(H_2)$ (10^4 cm^{-3})	$e\_n(H_2)$ (10^4 cm^{-3})	YSO
(1)	(2)	(3)	(4)	(5)	(6)	(7)	(8)	(9)	(10)	(11)	(12)	(13)
2	Rest	03 25 00.3	+30 44 10	26.0	-	13.53	0.07	0.6	-	0.16	-	
3	Rest	03 25 07.8	+30 24 22	9.2	0.2	11.39	0.06	46.0	2.0	12.32	0.5	
4	Rest	03 25 09.7	+30 23 53	9.2	0.2	11.51	0.1	53.0	3.0	14.20	0.8	
5	Rest	03 25 10.1	+30 44 41	10.0	0.2	12.34	0.05	26.0	2.0	6.96	0.5	
6	Rest	03 25 17.1	+30 18 53	10.3	0.4	12.28	0.07	12.0	2.0	3.21	0.5	
7	Rest	03 25 22.3	+30 45 09	12.06	0.08	14.87	0.38	54.0	1.0	14.46	0.3	YSO
8	Rest	03 25 26.2	+30 45 05	11.21	0.09	12.07	0.08	84.0	2.0	22.50	0.5	
9	Rest	03 25 26.9	+30 21 53	9.1	0.2	12.06	0.05	39.0	3.0	10.45	0.8	
10	Rest	03 25 32.3	+30 46 00	11.1	0.4	11.75	0.21	28.0	4.0	7.50	1.1	
11	Rest	03 25 35.5	+30 13 06	13.0	-	12.69	0.05	5.0	-	1.34	-	
12	Rest	03 25 36.2	+30 45 11	12.61	0.05	14.17	0.56	91.0	2.0	24.38	0.5	YSO
13	Rest	03 25 37.2	+30 09 55	15.0	-	13.24	0.05	7.0	-	1.88	-	
14	Rest	03 25 38.6	+30 43 59	14.05	0.09	21.42	0.65	55.0	1.0	14.73	0.3	YSO
15	Rest	03 25 46.1	+30 44 11	11.20	0.2	11.35	0.05	31.0	1.0	8.30	0.3	
16	Rest	03 25 47.5	+30 12 26	13.0	-	12.74	0.05	1.3	-	0.34	-	
17	Rest	03 25 48.8	+30 42 24	9.13	0.05	10.65	0.05	133.0	2.0	35.63	0.5	
18	Rest	03 25 50.6	+30 42 02	9.0	0.1	10.99	0.05	119.0	4.0	31.88	1.1	
19	Rest	03 25 55.1	+30 41 26	10.0	0.6	12.43	0.03	13.0	4.0	3.48	1.1	
20	Rest	03 25 56.4	+30 40 43	14.0	-	12.74	0.05	1.3	-	0.35	-	
21	Rest	03 25 58.5	+30 37 14	13.6	-	13.26	0.12	1.5	-	0.40	-	
22	Rest	03 26 37.0	+30 15 23	11.7	0.2	14.92	0.32	32.0	1.0	8.57	0.3	YSO
24	Rest	03 27 02.1	+30 15 08	10.4	0.4	12.57	0.06	13.0	2.0	3.48	0.5	
26	Rest	03 27 20.2	+30 04 26	18.0	-	15.44	0.1	7.0	-	1.88	-	
27	Rest	03 27 20.5	+30 00 42	20.0	-	14.4	0.1	1.0	-	0.27	-	
28	Rest	03 27 26.4	+29 51 08	18.0	-	13.51	0.09	3.0	-	0.80	-	
29	Rest	03 27 28.9	+30 15 04	10.7	0.2	11.81	0.04	27.0	1.0	7.23	0.3	
30	Rest	03 27 34.4	+30 09 22	13.0	-	12.18	0.06	9.0	-	2.41	-	
32	Rest	03 27 39.3	+30 12 59	13.05	0.07	15.54	0.34	48.2	0.9	12.91	0.2	YSO
33	Rest	03 27 40.0	+30 12 13	10.5	0.2	11.01	0.09	79.0	4.0	21.16	1.1	
34	Rest	03 27 41.9	+30 12 30	11.37	0.06	12.96	0.16	54.0	1.0	14.46	0.3	YSO
35	Rest	03 27 47.9	+30 12 02	11.9	0.1	12.59	0.16	32.0	1.0	8.57	0.3	YSO

Tabelle 2: Properties of cloud cores in Perseus

ID	Region	RA	DEC	T_{gas} (K)	e_T_{gas} (K)	T_{eff} (K)	e_T_{eff} (K)	$\Sigma(NH_3)$ (10^{13} cm^{-2})	$e\_\Sigma(NH_3)$ (10^{13} cm^{-2})	$n(H_2)$ (10^4 cm^{-3})	$e\_n(H_2)$ (10^4 cm^{-3})	YSO
(1)	(2)	(3)	(4)	(5)	(6)	(7)	(8)	(9)	(10)	(11)	(12)	(13)
36	Rest	03 27 55.9	+30 06 18	9.1	0.2	11.57	0.06	48.0	4.0	12.86	1.1	
37	Rest	03 28 00.7	+30 08 20	10.3	0.4	11.72	0.06	27.0	4.0	7.23	1.1	YSO
38	Rest	03 28 05.5	+30 06 19	9.4	0.3	11.06	0.07	44.0	3.0	11.79	0.8	
40	NGC1333	03 28 32.2	+31 11 09	10.8	0.1	14.15	0.11	41.0	1.0	10.98	0.3	YSO
41	NGC1333	03 28 32.4	+31 04 43	10.6	0.1	12.83	0.07	39.0	2.0	10.45	0.5	
42	Rest	03 28 33.4	+30 19 35	10.7	0.3	12.68	0.09	18.0	2.0	4.82	0.5	
43	NGC1333	03 28 34.1	+31 07 01	10.5	0.2	13.98	0.14	25.0	2.0	6.70	0.5	
44	NGC1333	03 28 36.3	+31 13 27	12.4	0.1	22.45	0.67	27.0	1.0	7.23	0.3	YSO
46	NGC1333	03 28 39.1	+31 06 00	10.54	0.09	12.83	0.07	56.0	2.0	15.00	0.5	YSO
47	NGC1333	03 28 39.5	+31 18 35	11.69	0.04	12.25	0.08	73.2	0.7	19.61	0.2	YSO
48	NGC1333	03 28 40.3	+31 17 56	11.7	0.1	12.59	0.07	91.0	4.0	24.38	1.1	YSO
49	Rest	03 28 41.7	+30 31 12	13.0	-	13.49	0.06	1.8	-	0.48	-	
50	NGC1333	03 28 42.6	+31 06 13	10.5	0.1	12.87	0.05	60.0	1.0	16.07	0.3	
51	NGC1333	03 28 46.0	+31 15 19	10.8	0.1	13.28	0.04	49.0	1.0	13.13	0.3	
52	NGC1333	03 28 48.5	+31 16 03	11.3	0.1	13.58	0.07	40.0	1.0	10.71	0.3	YSO
53	Rest	03 28 48.8	+30 43 25	17.0	-	14.37	0.08	0.9	-	0.24	-	
55	Rest	03 28 51.4	+30 32 58	19.0	-	14.54	0.07	11.0	-	2.95	-	
56	NGC1333	03 28 52.2	+31 18 08	13.8	0.2	14.05	0.09	20.0	1.0	5.36	0.3	YSO
57	NGC1333	03 28 55.2	+31 20 26	16.4	0.7	14.4	0.13	3.3	0.2	0.88	0.1	
58	NGC1333	03 28 55.3	+31 14 33	16.5	0.1	28.6	1.59	34.0	2.0	9.11	0.5	YSO
59	NGC1333	03 28 55.4	+31 19 19	14.5	0.1	15.09	0.09	28.0	1.0	7.50	0.3	YSO
60	Rest	03 28 56.2	+30 03 42	19.0	-	12.77	0.05	7.0	-	1.88	-	
61	NGC1333	03 28 57.5	+31 23 06	29.0	-	17.24	0.14	0.7	-	0.19	-	
63	NGC1333	03 28 58.6	+31 09 10	26.0	-	14.84	0.07	0.9	-	0.24	-	
64	NGC1333	03 28 59.6	+31 21 38	14.4	0.2	16.07	0.09	27.0	2.0	7.23	0.5	YSO
65	NGC1333	03 29 00.6	+31 11 59	12.5	0.1	15.05	0.2	37.0	1.0	9.91	0.3	YSO
66	NGC1333	03 29 01.4	+31 20 34	16.4	0.1	19.33	0.35	33.0	1.0	8.84	0.3	YSO
67	NGC1333	03 29 03.2	+31 15 59	16.3	0.2	20.79	0.53	41.0	2.0	10.98	0.5	YSO
68	NGC1333	03 29 03.4	+31 14 58	16.4	0.1	15.48	0.15	52.0	3.0	13.93	0.8	YSO
69	NGC1333	03 29 04.5	+31 18 43	13.6	0.2	14.95	0.12	25.0	1.0	6.70	0.3	
70	NGC1333	03 29 06.9	+31 15 44	14.8	0.2	12.93	0.09	46.0	2.0	12.32	0.5	
71	NGC1333	03 29 07.5	+31 21 54	23.0	2.0	25.45	0.25	1.2	0.1	0.32	0.0	YSO
72	NGC1333	03 29 07.8	+31 17 19	12.6	0.2	14.11	0.07	29.0	2.0	7.77	0.5	
73	NGC1333	03 29 08.9	+31 15 12	12.32	0.06	11.83	0.07	89.0	2.0	23.84	0.5	
75	NGC1333	03 29 10.3	+31 13 35	15.0	0.1	17	0.39	43.0	2.0	11.52	0.5	YSO
76	NGC1333	03 29 10.3	+31 21 44	35.0	-	31.04	0.43	1.5	-	0.40	-	YSO
77	NGC1333	03 29 11.4	+31 18 26	14.3	0.1	16.79	0.35	34.0	1.0	9.11	0.3	YSO
78	NGC1333	03 29 11.4	+31 13 07	13.5	0.7	16.13	0.67	40.0	1.0	10.71	0.3	YSO
79	NGC1333	03 29 14.9	+31 20 27	15.5	0.5	16.51	0.13	3.4	0.2	0.91	0.1	
81	NGC1333	03 29 17.2	+31 27 40	11.8	0.2	16.07	0.25	21.0	1.0	5.63	0.3	YSO
84	NGC1333	03 29 19.2	+31 23 28	13.3	0.4	19.64	0.21	15.0	2.0	4.02	0.5	YSO

Tabelle 2: Properties of cloud cores in Perseus

ID	Region	RA	DEC	T_{gas}	e_T_{gas}	T_{eff}	e_T_{eff}	$\Sigma(NH_3)$	$e\_\Sigma(NH_3)$	$n(H_2)$	$e\_n(H_2)$	YSO
				(K)	(K)	(K)	(K)	(10^{13} cm^{-2})	(10^{13} cm^{-2})	(10^{4} cm^{-3})	(10^{4} cm^{-3})	
(1)	(2)	(3)	(4)	(5)	(6)	(7)	(8)	(9)	(10)	(11)	(12)	(13)
85	NGC1333	03 29 20.5	+31 19 30	22.0	-	17.23	0.16	0.8	-	0.21	-	
86	NGC1333	03 29 22.5	+31 36 24	9.8	0.4	12.45	0.08	22.0	3.0	5.89	0.8	
87	NGC1333	03 29 22.9	+31 33 16	10.4	0.1	13.37	0.21	44.0	1.0	11.79	0.3	YSO
89	NGC1333	03 29 51.5	+31 39 12	10.5	0.1	14.38	0.28	39.0	1.0	10.45	0.3	YSO
90	NGC1333	03 30 13.6	+31 44 38	27.0	-	17.2	0.09	0.7	-	0.19	-	
91	Rest	03 30 15.1	+30 23 39	11.0	0.1	13.77	0.15	49.0	1.0	13.13	0.3	YSO
93	Rest	03 30 24.1	+30 27 39	10.5	0.2	13.63	0.09	14.0	1.0	3.75	0.3	
95	Rest	03 30 32.0	+30 26 19	10.01	0.06	12.31	0.1	106.0	2.0	28.39	0.5	YSO
96	Rest	03 30 45.6	+30 52 36	10.5	0.3	12.38	0.08	19.0	2.0	5.09	0.5	
97	Rest	03 30 50.5	+30 49 17	9.8	0.3	12.85	0.11	20.0	3.0	5.36	0.8	
98	Rest	03 31 14.4	+30 44 03	20.0	-	12.98	0.07	1.7	-	0.46	-	
99	Rest	03 31 20.0	+30 45 30	11.44	0.07	15.18	0.4	50.0	1.0	13.39	0.3	YSO
101	Rest	03 32 10.1	+31 19 54	23.0	-	15.35	0.12	6.0	-	1.61	-	
102	Rest	03 32 17.5	+30 53 58	26.0	-	14.5	0.07	0.8	-	0.21	-	
103	Rest	03 32 17.5	+30 49 49	11.7	0.09	12.27	0.28	62.0	1.0	16.61	0.3	YSO
104	Rest	03 32 26.9	+30 59 11	10.48	0.08	12.68	0.06	52.0	1.0	13.93	0.3	
105	Rest	03 32 28.1	+31 02 19	9.6	0.2	13.77	0.09	36.0	3.0	9.64	0.8	YSO
107	Rest	03 32 39.3	+30 57 29	13.0	-	13.93	0.05	2.7	-	0.72	-	
108	Rest	03 32 44.1	+31 00 01	10.16	0.09	12.89	0.03	72.0	2.0	19.29	0.5	
109	Rest	03 32 51.3	+31 01 48	11.2	0.4	13.49	0.03	11.0	2.0	2.95	0.5	
110	Rest	03 32 54.8	+31 19 23	18.0	-	15.19	0.06	1.1	-	0.29	-	
111	Rest	03 32 57.0	+31 03 21	10.1	0.1	12.64	0.07	43.0	1.0	11.52	0.3	
112	Rest	03 33 00.1	+31 20 45	11.2	0.5	13.99	0.05	11.0	3.0	2.95	0.8	
113	Rest	03 33 02.0	+31 04 33	10.0	0.1	11.87	0.03	61.0	2.0	16.34	0.5	
114	Rest	03 33 04.3	+31 04 57	9.86	0.06	11.78	0.03	106.0	2.0	28.39	0.5	
115	Rest	03 33 06.3	+31 06 26	10.3	0.5	12.3	0.04	33.0	4.0	8.84	1.1	
116	Rest	03 33 11.5	+31 17 23	16.0	-	14.48	0.07	17.0	-	4.55	-	
117	Rest	03 33 11.6	+31 21 33	17.0	-	15.69	0.07	1.3	-	0.35	-	YSO
118	Rest	03 33 13.3	+31 19 51	9.39	0.09	13.17	0.06	116.0	3.0	31.07	0.8	YSO
119	Rest	03 33 15.1	+31 07 04	11.52	0.04	12.49	0.1	100.0	1.0	26.79	0.3	YSO
121	Rest	03 33 17.9	+31 09 30	12.43	0.04	14.52	0.37	81.3	0.8	21.78	0.2	YSO
122	Rest	03 33 19.8	+31 22 41	22.0	-	16.52	0.07	0.8	-	0.21	-	
123	Rest	03 33 20.5	+31 07 37	11.71	0.05	12.09	0.12	113.0	1.0	30.27	0.3	YSO
124	Rest	03 33 25.2	+31 05 35	9.7	0.1	13.61	0.06	61.0	2.0	16.34	0.5	
125	Rest	03 33 25.4	+31 20 05	12.0	0.4	14.12	0.04	16.0	3.0	4.29	0.8	
126	Rest	03 33 27.1	+31 06 56	11.9	0.3	13.75	0.07	19.0	2.0	5.09	0.5	YSO
127	Rest	03 33 31.8	+31 20 02	10.9	0.3	14.56	0.06	22.0	3.0	5.89	0.8	
128	Rest	03 33 51.2	+31 12 38	10.7	-	15.03	0.09	13.0	-	3.48	-	YSO
129	Rest	03 33 52.5	+31 22 37	20.0	-	15.43	0.11	1.4	-	0.37	-	
132	Rest	03 35 21.5	+31 06 56	15.0	-	14.18	0.06	5.0	-	1.34	-	
139	Rest	03 38 15.1	+31 19 45	24.0	2.0	20.14	0.17	0.6	0.1	0.17	0.0	

Tabelle 2: Properties of cloud cores in Perseus

ID	Region	RA	DEC	T_{gas} (K)	e_T_{gas} (K)	T_{eff} (K)	e_T_{eff} (K)	$\Sigma(NH_3)$ (10^{13} cm^{-2})	$e\_\Sigma(NH_3)$ (10^{13} cm^{-2})	$n(H_2)$ (10^4 cm^{-3})	$e\_n(H_2)$ (10^4 cm^{-3})	YSO
(1)	(2)	(3)	(4)	(5)	(6)	(7)	(8)	(9)	(10)	(11)	(12)	(13)
141	IC348	03 40 14.5	+32 01 30	16.0	-	14.73	0.07	6.0	-	1.61	-	
142	IC348	03 40 49.5	+31 48 35	12.4	0.4	16.88	0.08	10.0	2.0	2.68	0.5	
144	IC348	03 41 19.9	+31 47 28	20.0	2.0	17.73	0.1	0.6	0.1	0.15	0.0	
145	IC348	03 41 40.2	+31 58 05	9.5	0.4	16.18	0.07	43.0	4.0	11.52	1.1	
146	IC348	03 41 45.2	+31 48 09	17.0	1.0	16.37	0.07	5.0	2.0	1.34	0.5	
147	IC348	03 41 46.0	+31 57 22	9.6	0.1	15.55	0.06	52.0	2.0	13.93	0.5	
148	IC348	03 41 58.3	+31 58 36	18.0	-	16.22	0.06	10.0	-	2.68	-	
150	IC348	03 42 20.3	+31 44 51	20.0	-	17.33	0.08	7.0	-	1.88	-	
151	IC348	03 42 24.0	+31 45 43	17.0	-	16.11	0.08	0.9	-	0.24	-	
152	IC348	03 42 47.2	+31 58 41	14.0	2.0	17.64	0.05	6.0	4.0	1.61	1.1	
153	IC348	03 42 52.5	+31 58 11	23.0	-	19.32	0.07	9.0	-	2.41	-	
154	IC348	03 42 57.3	+31 57 48	17.0	3.0	19.29	0.07	1.4	3.0	0.37	0.8	
156	IC348	03 43 38.1	+32 03 10	13.5	0.6	15.86	0.07	19.0	6.0	5.09	1.6	
158	IC348	03 43 45.5	+32 01 44	14.8	0.4	16.04	0.13	2.3	0.1	0.62	0.0	
159	IC348	03 43 45.8	+32 03 11	11.7	0.1	15.15	0.05	28.0	1.0	7.50	0.3	
160	IC348	03 43 50.5	+32 03 17	11.7	0.3	15.53	0.15	36.0	4.0	9.64	1.1	YSO
161	IC348	03 43 56.0	+32 00 45	12.9	0.3	14.61	0.28	40.0	3.0	10.71	0.8	
162	IC348	03 43 57.3	+32 03 04	14.2	0.6	16.83	0.28	13.0	4.0	3.48	1.1	YSO
163	IC348	03 43 57.8	+32 04 06	12.9	0.2	15.51	0.1	20.0	1.0	5.36	0.3	
164	IC348	03 44 01.7	+32 02 02	13.0	0.5	16.31	0.13	17.0	4.0	4.55	1.1	YSO
165	IC348	03 44 02.2	+32 02 32	11.1	0.1	15.31	0.08	41.0	2.0	10.98	0.5	YSO
166	IC348	03 44 02.3	+32 04 56	26.0	2.0	20.36	0.1	0.7	0.1	0.19	0.0	YSO
167	IC348	03 44 04.6	+31 58 07	21.0	-	16.64	0.05	1.1	-	0.29	-	
168	IC348	03 44 05.1	+32 00 28	11.0	2.0	16.1	0.1	7.0	7.0	1.88	1.9	YSO
169	IC348	03 44 05.3	+32 02 05	10.9	0.4	14.92	0.06	32.0	4.0	8.57	1.1	YSO
170	IC348	03 44 14.6	+31 57 59	10.6	0.6	15.44	0.08	21.0	5.0	5.63	1.3	
171	IC348	03 44 14.7	+32 09 11	12.9	0.4	18	0.11	8.0	2.0	2.14	0.5	
173	IC348	03 44 22.6	+31 59 24	10.5	0.4	15.03	0.08	33.0	4.0	8.84	1.1	YSO
174	IC348	03 44 22.6	+32 10 00	14.7	0.9	21.33	0.14	2.6	0.2	0.70	0.1	
176	IC348	03 44 36.4	+31 58 40	10.8	0.3	14.6	0.09	17.0	3.0	4.55	0.8	YSO
178	IC348	03 44 44.0	+32 01 24	16.0	1.0	17.44	0.34	2.7	0.3	0.72	0.1	YSO
180	IC348	03 44 48.8	+32 00 29	10.8	0.6	14.97	0.11	21.0	3.0	5.63	0.8	
181	IC348	03 44 56.1	+32 00 32	10.9	0.5	15.68	0.1	8.0	3.0	2.14	0.8	
182	IC348	03 45 10.7	+32 00 38	22.0	-	17.28	0.17	0.5	-	0.13	-	
183	IC348	03 45 15.9	+32 04 49	10.7	0.5	16.27	0.13	23.0	4.0	6.16	1.1	
188	Rest	03 47 33.5	+32 50 55	10.0	0.3	13.83	0.05	15.0	2.0	4.02	0.5	
189	Rest	03 47 38.6	+32 52 19	10.1	0.4	12.85	0.15	44.0	5.0	11.79	1.3	
190	Rest	03 47 39.7	+32 53 57	10.1	0.4	13.03	0.06	14.0	2.0	3.75	0.5	
191	Rest	03 47 39.8	+32 53 34	10.0	0.4	12.66	0.05	26.0	3.0	6.96	0.8	
192	Rest	03 47 41.4	+32 51 48	11.7	0.3	16.42	0.34	41.0	4.0	10.98	1.1	YSO

Notes: Col. (1): Identification number of the cloud cores. This is equivalent to NH3SCRïn Table 3 of Rosolowsky et al. (2008). Col. (2): Region of Persus in which the cloud cores are located. Positions outside of NGC1333 and IC348 are combined to Rest". Col. (3) and (4): Position of the cloud cores (J2000). Col.(5): Gas kinetic temperature from NH_3 line ratio measurements. For cores without a given error in T_{gas} this value represents an estimated upper limit. Col. (6): Error in T_{gas}. No error is given for cores where the NH_2(2,2) line could not be detected. Col. (7): Effective dust temperature. Col. (8): Error in effective dust temperature. Col. (9): Column density of NH_3. This value represents an estimated lower limit for cores without a given error in $\Sigma(NH_3)$. Col. (10): Error in $\Sigma(NH_3)$. For cores where the NH_2(2,2) line could not be detected no error is given. Col. (11): Volume density of H_2 calculated from $\Sigma(NH_3)$ using Eq. (6). Col. (12): Error in $n(H_2)$. Col. (13): Cores that contain at least one embedded source within $31''$ from their central position are labeled with "YSO".